

Chip-Scale Silicon Photonic Interconnects: A Formal Study on Fabrication Non-Uniformity

Mahdi Nikdast, *Member, IEEE*, Gabriela Nicolescu, *Member, IEEE*, Jelena Trajkovic, *Member, IEEE*, and Odile Liboiron-Ladouceur, *Senior Member, IEEE*

Abstract—Silicon photonic interconnect (SPI) is an attractive alternative for the power-hungry and low-bandwidth metallic interconnect in multiprocessor systems-on-chip (MPSoCs). When employing SPIs for wavelength-division multiplexing (WDM)-based applications, it is essential to precisely align the central wavelengths of different photonic devices (e.g., photonic switches) to achieve a reliable communication. However, SPIs are sensitive to fabrication nonuniformity (a.k.a. fabrication process variation), which results in wavelength mismatches between devices, and hence performance degradation in SPIs. This work presents a computationally efficient and accurate bottom-up approach to study the impact of fabrication process variations on passive silicon photonic devices and interconnects. We first model the impact of process variations at the component level (i.e., strip waveguides), then at the device level (i.e., add-drop filters and photonic switches), and finally at the system level (i.e., passive WDM-based SPIs). Numerical simulations are performed not only to evaluate the accuracy of our method, but also to demonstrate its high-computational efficiency. Furthermore, our study includes the design, fabrication, and analysis of several identical microresonators to demonstrate process variations in silicon photonics fabrication. The efficiency of our proposed method enables its application to large-scale passive SPIs in MPSoCs, where employing time-consuming numerical simulations is not feasible.

Index Terms—Fabrication non-uniformity, reliability, silicon photonic interconnects, wavelength-division multiplexing.

I. INTRODUCTION

THE inter- and intra-chip communication in multiprocessor systems-on-chip (MPSoCs) is growing rapidly due to the continuous increase in the integration density of processing cores on a single die. As a result, the metallic interconnect in MPSoCs fails to address the communication in such systems while respecting the system power budget and bandwidth requirements. Silicon photonic interconnect (SPI) is introduced as

Manuscript received January 10, 2016; revised April 18, 2016; accepted April 28, 2016. Date of publication May 04, 2016; date of current version July 22, 2016. This work was supported by Silicon Electronic-Photonic Integrated Circuits program (SIEPIC), Natural Sciences and Engineering Research Council (NSERC), and Regroupement Stratégique en MicroSystèmes du Québec (ReSMiQ).

M. Nikdast and G. Nicolescu are with the Department of Computer and Software Engineering, Polytechnique Montréal, Montréal, QC H3T 1J4, Canada (e-mail: mahdi.nikdast@polymtl; Gabriela.Nicolescu@polymtl.ca).

J. Trajkovic is with the Department of Electrical and Computer Engineering, Concordia University, Montréal, QC H3G 1M8, Canada (e-mail: jelena@ece.concordia.ca).

O. Liboiron-Ladouceur is with the Department of Electrical and Computer Engineering, McGill University, Montréal, QC H3A 0E9, Canada (e-mail: odile.liboiron-ladouceur@mcgill.ca).

Color versions of one or more of the figures in this paper are available online at <http://ieeexplore.ieee.org>.

Digital Object Identifier 10.1109/JLT.2016.2563781

a promising candidate to replace the low-performance metallic interconnect in MPSoCs, hence bringing lower power consumption, higher bandwidth, and lower latency to the communication in MPSoCs [1]. Moreover, employing wavelength-division multiplexing (WDM) can further boost the bandwidth performance of SPIs through simultaneous transmission of several optical wavelengths in a single waveguide.

Several WDM-based SPIs were proposed [2]–[5], in which waveguides and microresonators (MRs) are the primary building components. Achieving a reliable communication in SPIs, it is critical to align the central wavelengths of different photonic devices in such systems [6]. However, SPIs are sensitive to fabrication non-uniformity (a.k.a. fabrication process variation), resulting in wavelength mismatches among different devices, and hence performance degradation, or in the worst-case, system failure. Understanding process variations in SPIs helps develop system design strategies to compensate for variations (e.g., thermal tuning), as well as understand the implementation cost for such compensations (e.g., power consumption). Process variations stem from the optical lithography process imperfection, in which variations depend on the resist sensitivity, resist age or thickness, exposure change, and etching [7].

Numerical methods, such as the finite-difference time-domain [8], can be used to study the effect of process variations in silicon photonic devices. When designing a photonic device, sweeping the device design parameters (e.g., waveguide thickness and width) can help predict the behavior of the device after its fabrication, and hence help design a more robust device. In large-scale photonic interconnects consisting of hundreds and thousands of photonic devices, however, employing such numerical methods is not feasible as they impose an extremely high computation cost. The novel contribution of this paper is in developing a computationally efficient and accurate bottom-up approach to study the impact of fabrication process variations on passive silicon photonic devices and interconnects. The proposed approach is developed through employing and modifying analytical approximation methods for photonic components and devices. Our study employs a two-variable approach to take into account the variations in the top silicon thickness and waveguide width.

Considering detailed physical properties of photonic components, we first model the impact of process variations at the component level (i.e., strip waveguides), then at the device level (i.e., MR-based add-drop filters and switches), and finally at the system level (i.e., passive WDM-based SPIs). Numerical simulations are considered to evaluate the accuracy and computational efficiency of our proposed method. Compared with

numerical simulations, we demonstrate that our method has an average error rate smaller than 1% and a computation speed-up greater than $100\times$. Furthermore, our study includes the design, fabrication, and analysis of several identical MRs, to which we apply our proposed method to quantify different variations on the chip. The high efficiency of our proposed method enables system designers to evaluate the impact of fabrication process variations on large-scale photonic interconnects in MPSoCs. For instance, we apply our method in order to study the optical signal-to-noise ratio (OSNR) in a general passive WDM-based SPI under different process variations. The proposed general passive SPI can be applied to different passive SPI architectures.

We modeled the impact of process variations on strip waveguides and MR-based add-drop filters in [9]. The proposed models, however, were summarized without presenting the system level analytical models. In this paper, the process variation study considers the system level by comprehensively developing the required analytical models and theory for the whole system hierarchy (i.e., component, device, and system levels). Moreover, while this work aims at developing a systematic analytical method to study process variations in silicon photonic devices and interconnects, our work in [10] studied several fabricated MR-based all-pass filters to quantify the worst-case top silicon thickness variation and resonance wavelength shift. It is worth mentioning that rib waveguides are widely used for electro-optic devices (i.e., active silicon photonic devices) such as modulators, since they allow for electrical connections to be made to the waveguides (e.g., through p-n junctions). In addition to the variations in the silicon thickness and waveguide width, doping variations will also impact the performance of active devices based on rib waveguides. This paper only considers passive silicon photonic devices and integrated circuits in which the strip waveguide is the primary component.

The rest of the paper is organized as follows. Section II summarizes related work. An overview of the proposed bottom-up approach is presented in Section III. We study the impact of process variations on the strip waveguides in Section IV. Section V presents the analytical models developed to study MR-based add-drop filters and switches under process variations. Leveraging Sections IV and V, Section VI presents the general passive WDM-based SPI architecture and the study on its OSNR under fabrication process variations. We present the quantitative simulation results of our proposed models, as well as their evaluations against numerical simulations and our fabrication details in Section VII. Finally, Section VIII concludes our work.

II. RELATED WORK

Process variations have been mostly studied at the device level by analyzing the response of identically designed devices selected from a single die (i.e., within-die variations), from multiple dies on the same wafer (i.e., within-wafer variations), from different wafers (i.e., wafer-to-wafer variations), or even from different fabrication runs. Chrostowski *et al.* studied 371 identical racetrack resonators of $12\ \mu\text{m}$ radius fabricated on a $16 \times 9\ \text{mm}^2$ chip. Their study indicated a strong linear correlation between the resonance wavelength variations and the physical

distances of the MRs [6]. In [11], Zortman *et al.* quantified the source and impact of process induced resonant frequency variation for microdisk resonators, in which the frequency variation is the result of thickness and diameter variations alone, across individual dies, wafers, and wafer lots for separate process runs. By comparing the transverse electric (TE) and transverse magnetic (TM) resonant frequency variations in microdisk resonators, they demonstrated that the primary driver of the resonator non-uniformity in their fabrication process was the silicon-on-insulator (SOI) thickness variation, which could exceed 10 nm across a wafer [11]. They also found out that the sensitivity of both the TE and TM modes to the thickness variations is much larger than that to the width variations, while TM modes are considerably more sensitive to the thickness variations.

The manufacturing tolerance of over 500 four-channel microring resonators fabricated in a commercial 130 nm CMOS foundry using 193 nm lithography was analyzed and measured in [12]. The measured data gathered over multiple reticles, wafers, and fabrication lots indicated that the absolute resonance wavelengths of individual devices cannot be controlled across wafers or even across reticles or fields within a wafer. Chen *et al.* studied process variations in microring resonators, racetrack resonators, and directional couplers (DCs) all identically designed but fabricated through two different establishments (LETI and IMEC) [13]. They reported variations with the variances of 1.3, 1.3, and $0.33\ \text{nm}^2/\text{cm}$ in the responses of the microrings, racetrack resonators, and DCs, respectively.

In [14], [15], Selvaraja *et al.* indicated within-wafer silicon thickness non-uniformity of $\pm 20.68\ \text{nm}$ over a 200 mm SOI wafer. The same group also tried to alleviate process variations by improving the silicon thickness uniformity across the SOI wafer. Studying the die-to-die (i.e., within-wafer) non-uniformity in Bragg gratings fabricated using a CMOS-compatible process with 193 nm deep ultraviolet lithography, Wang *et al.* indicated that the wafer thickness variation considerably deviates the Bragg wavelength [16]. Beausoleil *et al.* at HP labs studied process variations in identically designed microring resonators, and reported a within-die variation with a variance of $0.5\ \text{nm}^2$ as well as a within-wafer variation with a variance of $2\ \text{nm}^2$ [17]. They attributed the changes in the silicon layer thickness and etch depth as the main contributor of such variations. In [18], an efficient stochastic collection (SC) method was proposed to analyze the variability of DCs.

Some efforts have also been made to explore and compensate for process variations at the system level. Xu *et al.* evaluated the bandwidth loss, which was shown to be more than 40%, in MR-based nanophotonic on-chip networks [19]. Improving the bandwidth, they proposed a method called MinTrim that is a channel remapping technique reducing the required thermal tuning power to correct the resonance wavelengths of MRs. The same group in [20] proposed a technique called BandArb to mitigate the effects of thermal and process variations on the bandwidth performance of silicon photonic networks by dynamically allocating the bandwidth at run-time based on demand and temperature. A reliability design flow to improve the reliability of photonic on-chip interconnects under process and thermal variations was proposed in [21], [22]. Using athermal coating at

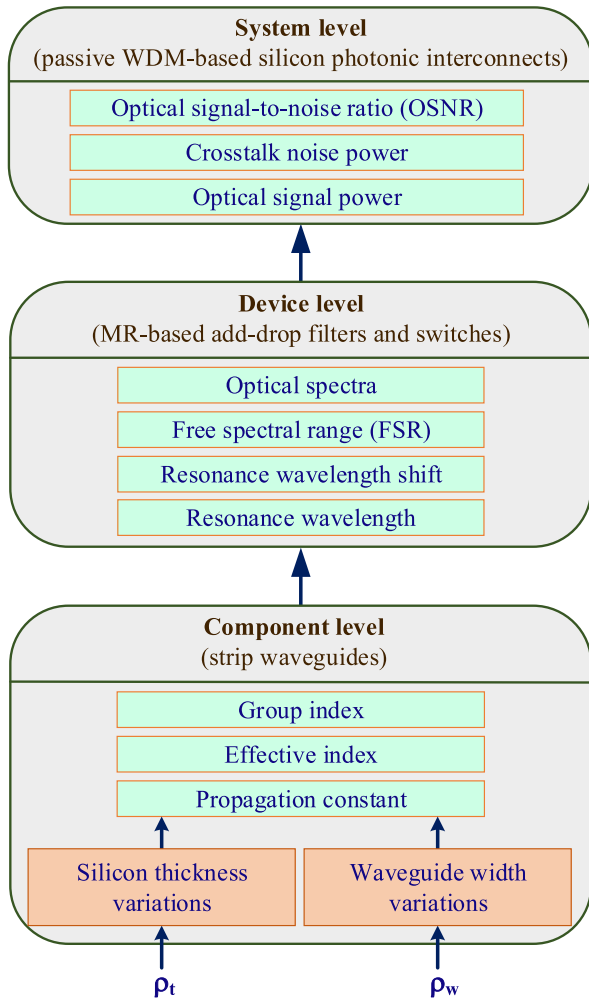


Fig. 1. Overview of the proposed bottom-up approach.

the fabrication level, voltage tuning at the device level, as well as channel remapping at the architecture level were proposed to compensate for the resonance wavelength shifts in the MRs under process and thermal variations.

Considering the aforementioned works in the device level domain, one can notice that the top silicon thickness variation is identified as the primary concern in silicon photonics fabrication and the primary driver of the MRs non-uniformity. Furthermore, regarding the work related to the system level domain, a comprehensive study on process variations is lacking that considers the impact on both silicon photonic devices and interconnects. It is worth mentioning that thermal and process variations are fundamentally different: the thermal variation is a result of thermo-optic effects on silicon photonic devices, while the process variation is caused by the lithography imperfection and etch non-uniformity of photonic devices.

III. PROPOSED METHODOLOGY

This section presents an overview of the proposed bottom-up approach to study the impact of fabrication process variations on passive WDM-based SPIs. As Fig. 1 indicates, we consider the

variations in the silicon thickness and waveguide width. In this paper, we define ρ_t and ρ_w to take into account the variations in the silicon thickness and waveguide width, respectively. These parameters can be assigned based on the variations quantified through different fabrications (e.g., the standard deviation of the silicon thickness or waveguide width on the chip). The proposed bottom-up approach starts by studying the impact of silicon thickness and waveguide width variations on the propagation constant as well as on the effective and group indices of strip waveguides. These parameters determine the propagation of light in photonic components and devices, and hence determine their characteristics. For example, the effective index of a strip waveguide in an MR determines the resonance wavelength of the MR, while the free-spectral range (FSR) of the MR is decided by the waveguide group index. Leveraging the analytical models at the component level, we study MR-based add-drop filters and switches under process variations. In particular, the impact of process variations ρ on the resonance wavelength and FSR of such devices are analytically modeled. Furthermore, the optical spectra of these devices are studied when the silicon thickness and waveguide width vary.

Considering the highest hierarchy of the proposed bottom-up approach, we study the impact of silicon thickness and waveguide width variations on passive WDM-based SPIs. At the system level, the power loss and crosstalk noise imposed by process variations are studied in a general passive SPI designed for WDM-based applications and supports n wavelengths. Moreover, the OSNR of the network is evaluated under random variations in the silicon thickness and waveguide width. In the following sections, an effort is made to detail the analytical models developed at the component, device, and system levels.

IV. PROCESS VARIATIONS AT COMPONENT LEVEL: STRIP WAVEGUIDES

Employing Marcatili's approach, which is an approximate analysis for calculating the propagation modes of waveguides [23], [24], we develop an analytical method to study the impact of process variations on the propagation constant as well as on the effective and group indices of the fundamental TE mode in strip waveguides (see Fig. 2). Please note that the analyses for the TM modes can be developed in a similar way, and thus has not been presented in this work.

Fig. 2(a) illustrates a 3D strip waveguide structure and its 2D approximation based on the proposed method is indicated in Fig. 2(b). Also, Fig. 2(c) depicts a cross-section of a strip waveguide. As can be seen from Fig. 2(b), the waveguide core, depicted as region I, is from silicon (Si) and has a rectangular cross-section with a thickness and width of t_s and w_s , respectively. The refractive index of the waveguide core is $n_{cr}(\lambda)$, which is a function of the input optical wavelength, as we discuss shortly. The core is covered by a cladding silicon oxide layer at the top with a refractive index of n_{cl} , and a substrate silicon oxide layer at the bottom with a refractive index of n_{sub} . In this work, we consider using symmetric strip waveguides, in which the homogeneous surrounding regions II, III, IV, and V are all of silicon dioxide (SiO_2) and have equal refractive

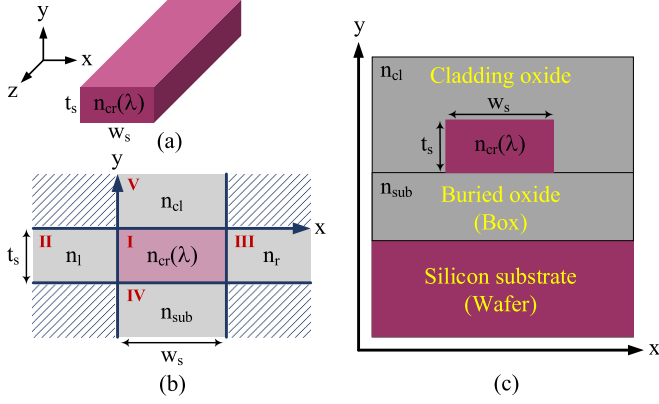


Fig. 2. (a) 3D strip waveguide structure; (b) 2D approximation of a strip waveguide; and, (c) cross-section of a strip waveguide.

indices of $n_l = n_r = n_{sub} = n_{cl} = 1.444$. The refractive index of the core is higher than those of the cladding and substrate, and hence the optical light is highly confined in the core of the waveguide. Also, the fields in the corners are neglected since they carry very little of the modes energy.

Given that the refractive index of a medium depends only on the x and y coordinates, we consider a monochromatic wave with an angular frequency ω propagating in the waveguide along the z direction with a propagation constant β . The resulting modal field is in the form of a standing wave in the core of the waveguide with an exponentially decaying field outside the core. As a result, an approximate solution to Maxwell's equations is obtainable. For a two-dimensional refractive index profile, $n(x, y)$, solutions of Maxwell's equations can be found in the form of [25]:

$$\mathcal{E}(x, y, z, t) = E(x, y)e^{i(\omega t - \beta z)}, \quad (1a)$$

$$\mathcal{H}(x, y, z, t) = H(x, y)e^{i(\omega t - \beta z)}, \quad (1b)$$

where \mathcal{E} and \mathcal{H} are the electric and magnetic fields, respectively. It is worth mentioning that, due to the spectral cutoff, the propagation constant β in the waveguide core is larger than the β in the surrounding regions. As a result, the light is highly confined in the core of the waveguide.

Maxwell's equations allow us to fully describe the electromagnetic fields (E_x, E_y, H_x , and H_y) in terms of the longitudinal field components (E_z and H_z). For each region j defined in Fig. 2(b) we have [25]:

$$E_{x/y} = \frac{-i}{K_j^2} \left(\beta \frac{\partial E_z}{\partial x/y} + / - \omega \mu_0 \frac{\partial H_z}{\partial y/x} \right), \quad (2a)$$

$$H_{x/y} = \frac{-i}{K_j^2} \left(\beta \frac{\partial H_z}{\partial x/y} - / + \omega \epsilon_0 n_j^2 \frac{\partial E_z}{\partial y/x} \right), \quad (2b)$$

where μ_0 and ϵ_0 are the permeability and the permittivity of free-space, respectively. Also, K_j can be defined as:

$$K_j^2 = n_j^2 k_0^2 - \beta^2, \quad (3)$$

in which k_0 is the free-space wavenumber and is equal to $\frac{2\pi}{\lambda}$, where λ is the optical wavelength. n_j is the refractive index

in region j , and β is the propagation constant. ω is the angular frequency and is equal to $\frac{2\pi c}{\lambda}$, in which c is the speed of light in free-space.

Based on Maxwell's equations, one can establish an equation for the longitudinal component of the electric field (E_z), and a similar equation for the longitudinal component of the magnetic field (H_z). These two equations are referred to as the reduced wave equations for strip waveguides:

$$\frac{\partial^2 E_z}{\partial x^2} + \frac{\partial^2 E_z}{\partial y^2} + K_j^2 E_z = 0, \quad (4a)$$

$$\frac{\partial^2 H_z}{\partial x^2} + \frac{\partial^2 H_z}{\partial y^2} + K_j^2 H_z = 0. \quad (4b)$$

The longitudinal field components of the modal electromagnetic field in each region are defined in a way that Maxwell's equations are obeyed in all the regions [24]. For region I, these components are in the form of:

$$E_z = a_1 \sin(k_x(x + \xi)) \cos(k_y(y + \eta)), \quad (5a)$$

$$H_z = a_2 \cos(k_x(x + \xi)) \sin(k_y(y + \eta)), \quad (5b)$$

where a_1 and a_2 are the amplitudes, k_x and k_y are the spatial frequencies, and ξ and η are the spatial shifts. Please note that for a symmetric strip waveguide the spatial shifts are small and can be ignored. Applying (5a) and (5b) to (2a) and (2b), and considering the wave equations in (4a) and (4b), the propagation constant in the waveguide core is calculated as:

$$K_I^2 = n_{cr}^2(\lambda)k_0^2 - \beta^2 = k_x^2 + k_y^2, \quad (6a)$$

$$\beta = \sqrt{n_{cr}^2(\lambda)k_0^2 - k_x^2 - k_y^2}. \quad (6b)$$

Finally, the effective index of the fundamental TE mode in strip waveguides, n_{eff} , is defined as:

$$n_{eff} = \frac{\beta}{k_0}. \quad (7)$$

Considering the propagation constant and effective index calculations in (6b) and (7), the effective index can be calculated based on the spatial frequencies k_x and k_y . Applying the boundary conditions (continuity of the fields) at the I-IV and I-V interfaces, where the dominant electric field component (E_x) is parallel to these interfaces, and the boundary conditions at the I-II and I-III interfaces, where the dominant electric field component is orthogonal to these interfaces, we can find the eigenvalue equations that help calculate the spatial frequencies k_x and k_y [24], [25]. Moreover, k_x and k_y depend on the width and thickness of the waveguide. As mentioned before, we define ρ_t and ρ_w to take into account the variations in the silicon thickness and waveguide width, respectively. Employing these parameters and respecting the boundary conditions, k_x and k_y can be calculated by solving the following eigenvalue equations:

$$e_{v1}(\lambda, W_s) = \tan(k_x W_s) - \frac{n_{cr}^2(\lambda)k_x (n_r^2 \gamma_l + n_l^2 \gamma_r)}{n_l^2 n_r^2 k_x^2 - n_{cr}^4(\lambda) \gamma_l \gamma_r}, \quad (8a)$$

$$e_{v2}(\lambda, T_s) = \tan(k_y T_s) - \frac{k_y (\gamma_{sub} + \gamma_{cl})}{k_y^2 - \gamma_{sub} \gamma_{cl}}, \quad (8b)$$

where

$$T_s = t_s \pm \rho_t, \quad (8c)$$

$$W_s = w_s \pm \rho_w, \quad (8d)$$

$$\gamma_{i/r}^2 = \left(n_{cr}^2(\lambda) - n_{i/r}^2 \right) k_0^2 - k_x^2, \quad (8e)$$

$$\gamma_{sub/cl}^2 = \left(n_{cr}^2(\lambda) - n_{sub/cl}^2 \right) k_0^2 - k_y^2. \quad (8f)$$

In order to accurately calculate the effective index of a strip waveguide, we need to take into account the impact of material dispersion and waveguide dispersion (chromatic dispersion). In particular, such dispersions play an important role when calculating the group index [7], as we discuss shortly. Material dispersion is caused by the variation of the index of refraction in a given material, silicon in this case, over the wavelength. Also, since the wavelength of the light is not that much larger than the core of the waveguide and $n_{cr}(\lambda) > n_{cl}$, part of the light is traveling slower in the geometric core of the waveguide and part of it is traveling faster in the cladding. This phenomenon is known as the waveguide dispersion. As the light is mostly confined in the waveguide core, we can ignore the dispersion in the substrate and cladding (regions IV and V in Fig. 2(b)). In this paper, we model the chromatic dispersion in silicon using the Sellmeier equation, which provides an empirical relationship between the refractive index of a medium and the light's wavelength [26]:

$$n_{cr}^2(\lambda) = 1 + \frac{10.67\lambda^2}{\lambda^2 - 0.31} + \frac{0.003\lambda^2}{\lambda^2 - 1.13} + \frac{1.54\lambda^2}{\lambda^2 - 1104^2}. \quad (9)$$

Considering the propagation constant calculation in (6b), the effective index of a strip waveguide under silicon thickness and waveguide width variations, and when the optical wavelength is λ is calculated in:

$$n_{eff}(T_s, W_s, \lambda) = \frac{\lambda}{2\pi} \sqrt{n_{cr}^2(\lambda)k_0^2 - k_x^2(T_s, W_s, \lambda) - k_y^2(T_s, W_s, \lambda)}. \quad (10)$$

Please note that based on (8a) and (8b), k_x and k_y depend on the waveguide thickness and width as well as the optical signal wavelength in (10). The group index describes the velocity at which the envelope of a propagating pulse travels and is a characteristic of a dispersive waveguide. As mentioned before, it is an important metric that determines the FSR and the resonance wavelength shift in MRs. Considering both the material and waveguide dispersion and the effective index definition in (10), the group index, n_g , of a strip waveguide under different variations can be defined as:

$$n_g(T_s, W_s, \lambda) = n_{eff}(T_s, W_s, \lambda) - \lambda \frac{dn_{eff}(T_s, W_s, \lambda)}{d\lambda}. \quad (11)$$

V. PROCESS VARIATIONS AT DEVICE LEVEL: MR-BASED ADD-DROP FILTERS AND SWITCHES

Leveraging the proposed analytical models in the previous section, we study the impact of process variations on MR-based add-drop filters and switches in this section. In this paper, we

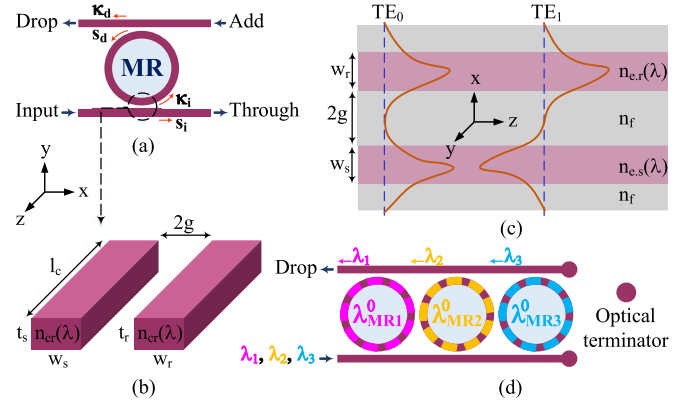


Fig. 3. (a) MR-based add-drop filter structure; (b) 3D DC model for the coupling region in MR-based add-drop filters; (c) 2D approximation of the coupler including the symmetric (TE_0) and antisymmetric (TE_1) supermodes; and, (d) passive WDM-based photonic switch.

consider racetrack MRs and for simplicity we refer to them as MRs. MR-based add-drop filters are the basic building blocks in passive SPIs which can, when on resonance, switch/drop an optical signal from the input to the drop port (see Fig. 3(a)), or let it pass from the input towards the through port. Therefore, such filters should be able to drop/switch an optical signal at a specific wavelength and any deviation in this process can result in performance degradation. Nevertheless, process variations shift the resonance wavelengths of MRs [6], resulting in optical loss and crosstalk noise when switching optical signals. This section develops the analytical models required to study the resonance wavelength shift and optical spectra of MR-based add-drop filters and switches.

A. Resonance Wavelength Shift

Fig. 3(a) depicts the structure of an MR-based add-drop filter. As the figure indicates, a portion of the input optical signal couples to the MR with a cross-over coupling coefficient of κ_i , and then it couples to the drop waveguide with a coupling coefficient of κ_d . Similarly, the uncoupled light continues propagating towards the through port and inside the MR with straight-through coefficients of s_i and s_d , respectively [27]. In this paper, we assume that the input and drop waveguides are symmetrically coupled to the MR, i.e., $\kappa_i = \kappa_d$ and $s_i = s_d$.

When the round-trip optical phase, ϕ_{rt} , is an integer multiple of 2π , the MR is on resonance and it drops the input signal:

$$\phi_{rt}(T_r, W_r, \lambda_{MR}) = \frac{2\pi n_{eff}(T_r, W_r, \lambda_{MR})L_{rt}(T_r, W_r)}{\lambda_{MR}} = m2\pi, \quad (12)$$

in which T_r and W_r , respectively, indicate the thickness and width of the MR's waveguide under variations, and they can be defined similarly to (8c) and (8d). We can safely assume that $T_r = T_s$ and $W_r = W_s$, i.e., while $t_r = t_s$ and $w_r = w_s$, the variations in the input waveguide and the MR are also the same. m is an integer number that denotes the order of the resonant mode, and λ_{MR} is the m th-order resonance wavelength of the

MR. Also, L_{rt} is the round-trip length of the MR that equals $2\pi r(T_r, W_r) + 2l_c$, where $r(T_r, W_r)$ is the MR's radius under variations and l_c is the coupler length (see Fig. 3(b)). It is worth mentioning that the effective and group indices of the MR can be calculated using the input waveguide. Fig. 3(d) indicates a passive WDM-based photonic switch in which the MRs are on resonance (i.e., optical signals on different wavelengths, which are matched with the resonance wavelengths of the MRs, are dropped).

Analyzing the resonance wavelength shift in an MR, we need to take into account the impact of waveguide dispersion [27]. As the n_{eff} changes, the resonance wavelength shifts, which results in an alteration in n_{eff} due to the non-zero slope of $\frac{\partial n_{eff}}{\partial \lambda}$. Considering the first order approximation of the waveguide dispersion and the relations in (11) and (12), the resonance wavelength shift, $\Delta\lambda_{MR}$, is calculated as:

$$\Delta\lambda_{MR}(T_r, W_r, \lambda_{MR}^0) = \frac{\Delta_{\rho_{t/w}} n_{eff} \lambda_{MR}^0}{n_g(t_r, w_r, \lambda_{MR}^0)}, \quad (13)$$

where $\Delta_{\rho_{t/w}} n_{eff}$ includes the changes in the effective index due to the thickness or waveguide width variations. Also, λ_{MR}^0 is the initial resonance wavelength with no variations. The FSR, which is the wavelength range between two resonances, as a function of the resonance wavelength and under different variations is given by:

$$FSR(T_r, W_r, \lambda_{MR}) = \frac{\lambda_{MR}^2}{n_g(T_r, W_r, \lambda_{MR}) L_{rt}(T_r, W_r)}. \quad (14)$$

As the equation indicates, the FSR will get wider or narrower as a result of silicon thickness and waveguide width variations.

B. Optical Spectra of MR-Based Add-Drop Filters and Switches

In this section, we study the impact of process variations on the optical spectra of MR-based add-drop filters and switches. As the resonance wavelength shifts, an optical signal cannot be completely coupled into the MR, or in the worst-case, it can be coupled into a neighboring channel. Such deviations cause performance degradation by introducing power loss (the former case) and crosstalk (the latter case), as we discuss in details in the next section.

We start by studying the impact of process variations on the coupling mechanism of MR-based add-drop filters. Studying the cross-over and straight-through coefficients, $\kappa_{i/d}$ and $s_{i/d}$, we model the coupling region in Fig. 3(a), the region specified by a dashed circle, in Fig. 3(b). As the figure indicates, the coupling region can be studied by considering a DC, in which two identical strip waveguides are in close proximity. The gap between the two waveguides is $2g$, which decreases (increases) as the waveguides get wider (narrower). We analytically calculate the cross-over length, L_c , and the coefficients using the supermode theory [7], [28]. The cross-over length is a length over which the optical power completely couples from one waveguide to the other one after a π phase shift difference. As a result, for any length l_c shorter than L_c , a fraction of the optical power (i.e., $\kappa_{i/d}^2$) couples from one waveguide to the other

one, while the rest of the power (i.e., $s_{i/d}^2$) remains in the first waveguide.

Supermode analysis studies waveguides by considering the interfaces of the modes of the total structure. Compared to the coupled mode theory, supermode analysis is more accurate when the separation between two waveguides is small (e.g., 200 nm) [28]. According to the supermode analysis, the effective indices of the first two eigenmodes of the coupled waveguides, which are known as symmetric (even) and antisymmetric (odd) modes (see Fig. 3(c)), determine the cross-over length and coupling coefficients in a DC. Given that the effective index of the symmetric mode is n_{sm} and the effective index of the antisymmetric mode is n_{asm} , the cross-over length can be calculated as:

$$L_c(T_r, W_r, \lambda) = \frac{\lambda}{2(n_{sm}(T_r, W_r, \lambda) - n_{asm}(T_r, W_r, \lambda))}, \quad (15)$$

in which $n_{sm} > n_{asm}$. Accordingly, the cross-over coupling coefficient is defined as:

$$\kappa_{i/d}(T_r, W_r, \lambda) = \left| \sin\left(\frac{\pi}{2L_c(T_r, W_r, \lambda)} l_c\right) \right|, \quad (16)$$

where l_c is the length of the coupler. We assume a lossless coupler in which $|\kappa_{i/d}|^2 + |s_{i/d}|^2 = 1$, but the optical losses of the coupler are included in the round-trip loss of the entire optical cavity. Calculating n_{sm} and n_{asm} , we approximate the 3D DC in Fig. 3(b) with the 2D structure shown in Fig. 3(c). In this figure, $n_{e,r}(\lambda) = n_{e,s}(\lambda)$ is the effective index of the slab waveguide with a thickness T_r in the y direction in Fig. 3(b), which can be calculated using the proposed method in the previous section. Furthermore, we consider $n_f = 1.444$. Finally, the effective index of the symmetric supermode can be calculated using the following eigenvalue equation:

$$e_{v3}(\lambda, W_r, g) = \tan(2N_1) - \frac{N_1 N_2 (1 + \tanh(2N_2 g W_r^{-1}))}{N_1^2 - N_2^2 \tanh(2N_2 g W_r^{-1})}, \quad (17a)$$

$$2N_1 = k_0 W_r \sqrt{n_{e,r}^2(\lambda) - (\beta/k_0)^2}, \quad (17b)$$

$$2N_2 = k_0 W_r \sqrt{(\beta/k_0)^2 - n_f^2}, \quad (17c)$$

in which for the antisymmetric mode \tanh should be replaced by \coth [29].

Employing the coupling coefficients, we can analyze the power transforms in an add-drop filter. Considering the time-domain coupling theory [30], [31], the transmission from the input port to the through port under variations is given by:

$$Th(T_r, W_r, \lambda) = \frac{s_{i/d}(T_r, W_r, \lambda) - s_{i/d}^*(T_r, W_r, \lambda) \sqrt{A} e^{i\phi_{rt}}}{1 - \sqrt{A} s_{i/d}^{*2}(T_r, W_r, \lambda) e^{i\phi_{rt}}}, \quad (18a)$$

while the power on the drop port can be calculated as:

$$Dr(T_r, W_r, \lambda) = \frac{-\kappa_{i/d}^*(T_r, W_r, \lambda) \kappa_{i/d}(T_r, W_r, \lambda) A^{1/4} e^{i\frac{\phi_{rt}}{2}}}{1 - \sqrt{A} s_{i/d}^{*2}(T_r, W_r, \lambda) e^{i\phi_{rt}}}. \quad (18b)$$

In these equations, $*$ is the complex conjugation. A is the power attenuation that can be calculated as $A(T_r, W_r) =$

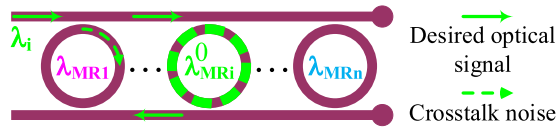


Fig. 4. MR-based photonic switch for passive WDM-based SPIs consisting of n MRs to simultaneously switch n different wavelengths.

$e^{-L_p L_{rt}(T_r, W_r)}$, in which L_p is the propagation loss of the waveguide in dB/cm. Please note that the total round-trip phase, ϕ_{rt} calculated in (12), includes the phase accumulated in the light propagating in the coupler. In the case of an all-pass filter, which consists of an input waveguide coupled to an MR, we can calculate the through-port response as:

$$Th_{ap}(T_r, W_r, \lambda) = \frac{-\sqrt{A} + s_{i/d}(T_r, W_r, \lambda)e^{-i\phi_{rt}}}{-\sqrt{A}s_{i/d}^*(T_r, W_r, \lambda) + e^{-i\phi_{rt}}}. \quad (19)$$

As can be seen from (18a) and (18b), all the parameters that determine the optical spectrum of an MR-based add-drop filter are affected by process variations (see also (12) and (16)).

VI. PROCESS VARIATIONS AT SYSTEM LEVEL: PASSIVE WDM-BASED SILICON PHOTONIC INTERCONNECTS

Leveraging the proposed analytical models at the component and device levels, we now study the impact of fabrication process variations on passive WDM-based SPIs in this section. In particular, we are interested to find out how the OSNR in SPIs are affected by the variations in the silicon thickness and waveguide width. We start by analyzing an MR-based photonic switch, shown in Fig. 4, which is the building block in passive WDM-based SPIs. As the figure indicates, the considered photonic switch is capable of simultaneously switching n different wavelengths through n MRs. It is worth mentioning that each MR's radius r is slightly different to cover the whole considered wavelength range. An optical signal on the wavelength λ_i passes MRs with $\lambda_{MRj} \neq \lambda_i$ (i.e., the input signal wavelength and the MR resonance wavelength are different), and then it couples into the MR with $\lambda_{MRi'}^0 = \lambda_i$ (i.e., the input signal wavelength and the MR resonance wavelength are the same). Note that $1 \leq i, i', j \leq n$. Here, i equals i' when there are no variations, and it can be different from i' when variations are introduced. Moreover, all along this path, the optical signal suffers from power loss caused by passing and coupling into MRs (i.e., passing loss and dropping loss) as well as the power loss caused by the waveguide propagation loss.

Considering Fig. 4 and (18a) and (18b), the power loss imposed on the desired optical signal on the wavelength λ_i is

calculated as:

$$\overrightarrow{L_{sw}}(T_r, W_r, \lambda_i) = Th(T_r, W_r, \lambda_i, MR_j)^{2(i'-1)} Dr(T_r, W_r, \lambda_i, MR_{i'}) L_p^{d_1(i')}. \quad (20)$$

In this equation, the propagation loss, $L_p^{d_1}$, can be calculated by estimating the distance that the optical signal has traveled in a photonic switch (i.e., d_1 in the equation). For the optical signal on the wavelength λ_i dropped to the MR with $\lambda_{MRi'}^0$, d_1 can be estimated as $d_1(i') = 2r_j(2i' + 1) + 2i'l_c$ and $1 \leq j \leq i'$. Please note that the fourth input parameter in $Th(T_r, W_r, \lambda_i, MR_j)$ indicates the MR number from which the optical signal passes. Similarly, $MR_{i'}$ in $Dr(T_r, W_r, \lambda_i, MR_{i'})$ denotes the MR number to which the optical signal drops. $\overrightarrow{L_{sw}}(T_r, W_r, \lambda_i)$ indicates the power loss imposed on the desired optical signal on the wavelength λ_i . The arrow indicates the direction that the optical signal travels in the photonic switch: it uses a port on the left to enter the photonic switch. It is important to consider the direction of the optical signal to accurately develop the models when considering process variations at the system level, as we discuss shortly. Similarly, when an optical signal of the wavelength λ_i enters a photonic switch from a port on the right, the imposed power loss is defined as:

$$\overleftarrow{L_{sw}}(T_r, W_r, \lambda_i) = Th(T_r, W_r, \lambda_i, MR_j)^{2(n-i')} Dr(T_r, W_r, \lambda_i, MR_{i'}) L_p^{d_2(i')}, \quad (21)$$

in which d_2 can be estimated as $d_2(i') = 2(n - i' + 1)(2r_j + l_c) + 2r_j$ and $i' \leq j \leq n$.

When an optical signal passes a photonic switch, not only does it suffer from power loss, but also some crosstalk noise interferes with that optical signal (see Fig. 4). We consider in-band crosstalk (i.e., when the optical crosstalk noise is at the same wavelength as the desired optical signal) which is of critical concern because it cannot be removed by filtering. Within the in-band crosstalk, the first-order coherent crosstalk noise, whose phase is correlated with the desired optical signal, is considered. Considering Fig. 4, a portion of the optical signal on the wavelength λ_i couples into the MRs with λ_{MRj} and $1 \leq j < i'$, and then it interferes with the desired optical signal as coherent crosstalk noise on the drop port. We consider the worst-case scenario in which the crosstalk noise from each MR can be added together [32]. Considering (18a) and (18b), the coherent crosstalk noise interfered with the desired optical signal entered through a left-hand-side port can be calculated as (22) (see bottom of the page). Similarly, when the desired

$$\overrightarrow{X_{sw}}(T_r, W_r, \lambda_i) = \sum_{k=1}^{i'-1} \left(Th(T_r, W_r, \lambda_i, MR_{1:k-1})^{2(k-1)} Dr(T_r, W_r, \lambda_i, MR_k) \right) L_p^{d_1(k)}. \quad (22)$$

$$\overleftarrow{X_{sw}}(T_r, W_r, \lambda_i) = \sum_{k=i'+1}^n \left(Th(T_r, W_r, \lambda_i, MR_{k+1:n})^{2(n-k)} Dr(T_r, W_r, \lambda_i, MR_k) \right) L_p^{d_2(k)}. \quad (23)$$

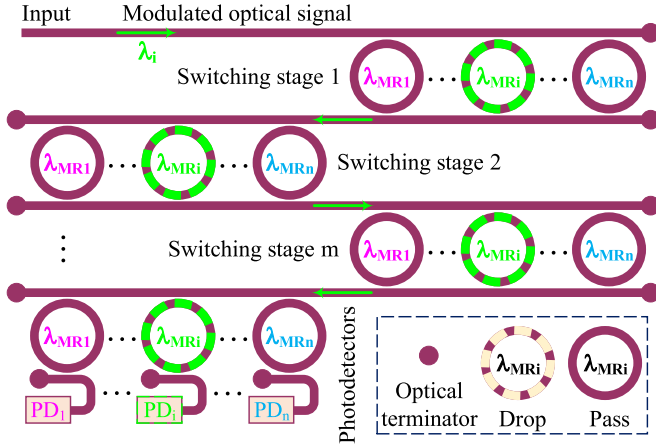


Fig. 5. General passive WDM-based SPI for WDM-based applications supporting n wavelengths. It has m switching stages with n MRs at each stage. All the functional devices utilize MRs, including wavelength-selective photodetectors and photonic switches.

optical signal enters a port on the right-hand-side of a photonic switch, the accumulated crosstalk noise on the drop port can be calculated as (23) (see bottom of the previous page).

Leveraging the power loss and crosstalk noise models developed for WDM-based photonic switches, we model the signal power and crosstalk noise power in passive WDM-based SPIs. Fig. 5 illustrates a general passive WDM-based SPI supporting n different wavelengths. It consists of m switching stages where each stage includes n MRs (i.e., $m \times n$ MRs in total). Optical terminators (e.g., waveguide tapers) are included to avoid the optical signal reflecting back on the waveguides. The general architecture can be applied to any specific passive SPI: in any architecture, the optical signal is routed through a number of MRs ($m \times n$ MRs in our general model), and it is ultimately detected at the photodetectors (n photodetectors in our general model) located at the end of the communication line. As a result, the models developed in this section can be applied to study process variations in different optical interconnect architectures [2]–[5].

We start by analyzing the desired signal power received at the photodetectors. Considering Fig. 5, an optical signal on the wavelength λ_i passes the MRs with $\lambda_{MRj} \neq \lambda_i$, couples into the MRs with $\lambda_{MRi'}^0 = \lambda_i$, dropped through the MR with $\lambda_{MRi'}^0 = \lambda_i$ on the stage $m + 1$, and finally is detected by the photodetector PD_i ($1 \leq i, i', j \leq n$). This communication can be seen as a communication between two processing cores in an MPSoC. Considering (20) and (21), the desired signal power received at the photodetector PD_i under different variations can

be calculated as:

$$P(T_r, W_r, \lambda_i) = P_{in} \overrightarrow{L_{sw}}(T_r, W_r, \lambda_i)^{\lceil \frac{m}{2} \rceil} \overleftarrow{L_{sw}}(T_r, W_r, \lambda_i)^{\lfloor \frac{m}{2} \rfloor} L_{PD}(T_r, W_r, \lambda_i), \quad (24a)$$

in which P_{in} is the optical power at the input port in Fig. 5, and $L_{PD}(T_r, W_r, \lambda_i)$ is the power loss associated with the photodetector PD_i , which is given by:

$$L_{PD}(T_r, W_r, \lambda_i) = Th(T_r, W_r, \lambda_i, MR_j)^a Dr(T_r, W_r, \lambda_i, MR_{i'}) L_p^{d_3}, \quad (24b)$$

in which $a = (m \bmod 2)(n - i') + ([m + 1] \bmod 2)(i' - 1)$, $d_3 = (a + 1)(2r_j + l_c) + 2r_j$, and $1 \leq j \leq n$. The crosstalk noise power, $X_P(T_r, W_r, \lambda_i)$, interfered with the desired optical signal on the wavelength λ_i and received at the photodetector PD_i under different variations can be calculated as (25) (see bottom of the page).

Utilizing (24a), (24b), and (25), we define the optical SNR (in dB) as the ratio between the desired optical signal power on the wavelength λ_i and the crosstalk noise power corrupting that signal received at the photodetector PD_i :

$$OSNR(T_r, W_r, \lambda_i) = 10 \log_{10} \frac{P(T_r, W_r, \lambda_i)}{X_P(T_r, W_r, \lambda_i)}. \quad (26)$$

It is worth mentioning that the impact of other kinds of noise existing in SPIs (e.g., thermal noise, shot noise, and dark noise) can be added to the analytical models proposed in this section.

VII. QUANTITATIVE SIMULATION RESULTS, EVALUATIONS, AND FABRICATION

In this section, we quantitatively simulate our proposed models in MATLAB. Evaluating the proposed method, we perform numerical simulations in MODE, which is a commercial-grade simulator eigenmode solver and propagator developed by Lumerical [33]. Moreover, our fabrication and its results are detailed in this section, to which the proposed method is applied to quantify the worst-case variations. We consider strip waveguides with a width of $w_r = w_s = 500$ nm and a thickness of $t_r = t_s = 220$ nm (see Fig. 3(b)). Furthermore, similar to our fabrication, we consider the central laser wavelength, λ , and the gap, $2g$, to be 1550 nm and 200 nm, respectively. In this paper, we assume that $L_p = 2$ dB/cm [34]. The results are shown for the fundamental TE mode.

$$X_P(T_r, W_r, \lambda_i) = P_{in} \sum_{l=1}^m \left((l \bmod 2) \frac{P(T_r, W_r, \lambda_i)}{P_{in} \overrightarrow{L_{sw}}(T_r, W_r, \lambda_i)} \overrightarrow{X_{sw}}(T_r, W_r, \lambda_i) \right) + P_{in} \sum_{l=1}^m \left(([l + 1] \bmod 2) \frac{P(T_r, W_r, \lambda_i)}{P_{in} \overleftarrow{L_{sw}}(T_r, W_r, \lambda_i)} \overleftarrow{X_{sw}}(T_r, W_r, \lambda_i) \right). \quad (25)$$

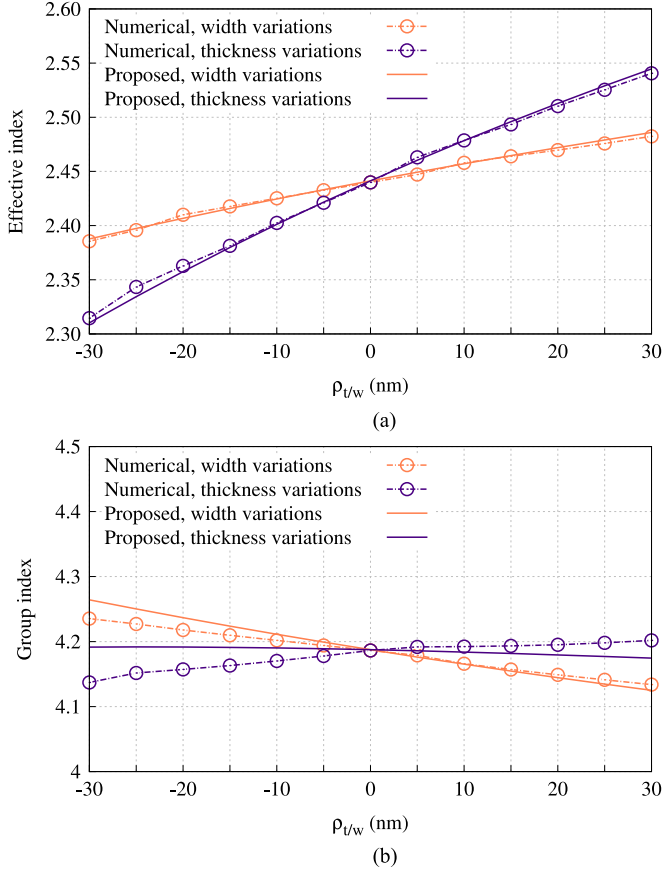


Fig. 6. Effective and group indices of a strip waveguide calculated using MODE (dashed line with circles) and the proposed method (solid line) under silicon thickness and waveguide width variations ($\rho_{t/w} \in [-30, 30]$ nm). (a) Effective index; and, (b) group index.

A. Component and Device Levels Results

This section presents the quantitative simulation results of the proposed models at the component and device levels (Sections IV and V). In this section, a variation range of ± 30 nm is considered (i.e., $\rho_{t/w} \in [-30, 30]$ nm). It is worth mentioning that to better indicate the impact of each variation on the different properties of strip waveguides and add-drop filters, we first consider applying each variation separately (i.e., ρ_t or ρ_w) while performing the simulations in this section.

Employing (10) and (11), Fig. 6 depicts the effective and group indices of a strip waveguide under silicon thickness and waveguide width variations (i.e., thickness varies between 190 nm and 250 nm, while the waveguide width changes between 470 nm and 530 nm). The x-axis indicates the variation range for both the silicon thickness and waveguide width. As can be seen, when $\rho_{t/w}$ increases, the effective index in Fig. 6(a) increases. The group index shown in Fig. 6(b), however, remains almost the same when ρ_t increases while it slightly decreases as ρ_w increases. The group indices changes under thickness and waveguide width variations can be explained based on (11) and considering the effective indices variations in Fig. 6(a). Considering Fig. 6, we can notice that the impact of silicon thickness variations on the effective and group indices is more important than that of waveguide width variations. This observation is in

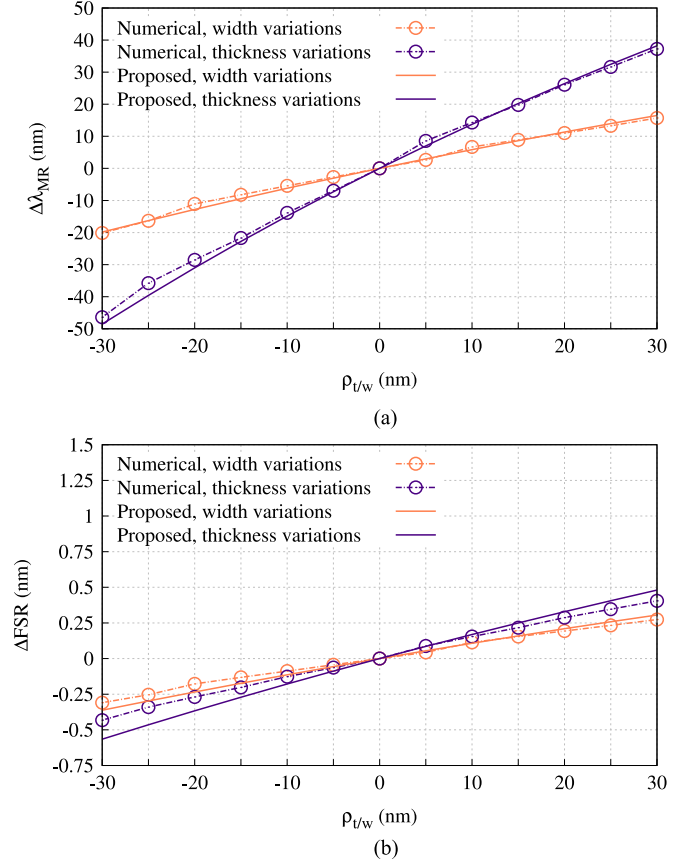


Fig. 7. Resonance wavelength shift and FSR variations in MRs under silicon thickness and width variations. In (a) the resonance wavelength shift is independent of the MR's radius. (a) Resonance wavelength shift; and (b) FSR variations ($r \approx 9 \mu\text{m}$ and $l_c = 4 \mu\text{m}$).

agreement with the demonstrations in [6], [11], [15] (see our discussion in Section II). Furthermore, comparing the numerical simulation results with those from our method, we observe a high accuracy of our proposed method with an average error rate smaller than 1%.

The changes in the effective and group indices vary the resonance wavelength and the FSR of MRs. Based on (13), Fig. 7(a) illustrates the resonance wavelength shift in MRs under the variations in the silicon thickness and waveguide width. The resonance wavelength shift in this figure does not depend on the MR's radius. The original resonance wavelength, λ_{MR}^0 , is 1550 nm. As Fig. 7(a) indicates, when there are no variations (i.e., $\rho_t = \rho_w = 0$) the resonance wavelength does not vary. When the silicon thickness or waveguide width variations are introduced, the resonance wavelength shifts almost linearly with respect to those variations. When $\rho_{t/w} < 0$, there is a blue-shift in the resonance wavelength, while a red-shift is observable when $\rho_{t/w} > 0$. Furthermore, as expected, the impact of the silicon thickness variations is more severe compared with that of the waveguide width variations: in the worst-case, when $\rho_{t/w} \in [-30, 30]$ nm, the silicon thickness variation can result in a ≈ 90 nm shift in the resonance wavelength of the MR, while the waveguide width variations shift the resonance wavelength by ≈ 40 nm. Considering Fig. 7(a), $\frac{\Delta\lambda_{MR}}{\Delta\rho_t} = 1.4$ and $\frac{\Delta\lambda_{MR}}{\Delta\rho_w} = 0.6$.

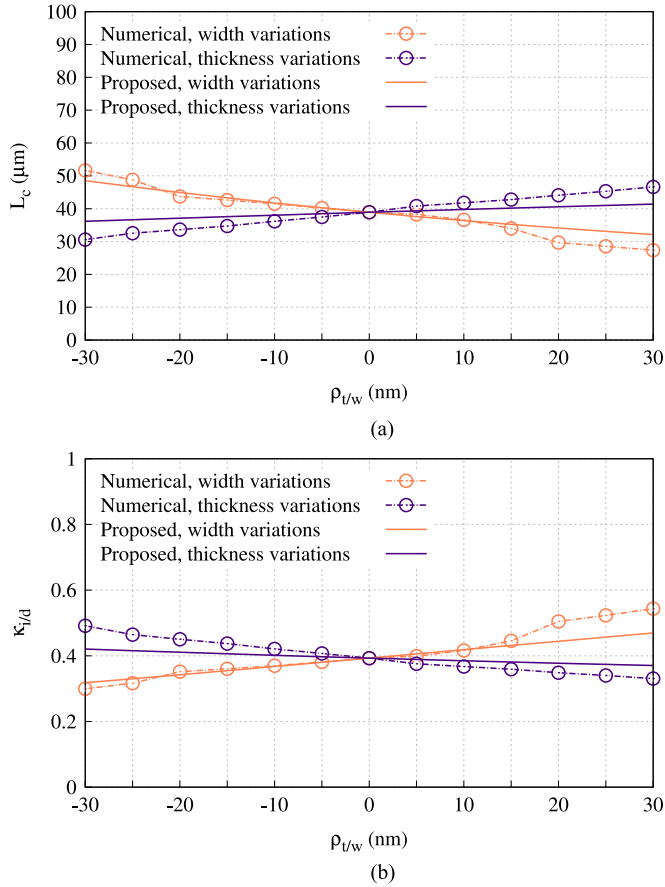


Fig. 8. Cross-over length and cross-over coupling coefficient of a DC with a length of $l_c = 10 \mu\text{m}$ under variations in the silicon thickness and waveguide width. (a) Cross-over length; and, (b) cross-over coupling coefficient ($l_c = 10 \mu\text{m}$).

Utilizing (14), the impact of silicon thickness and waveguide width variations on the FSR of an MR with a radius of $\approx 9 \mu\text{m}$ and a coupler length of $4 \mu\text{m}$ is depicted in Fig. 7(b). Please note that the MR's radius and the coupler length are considered only as an example. Over the considered variation range, the silicon thickness variations change the FSR of the MR by $\approx 1 \text{ nm}$ in the worst-case, while the impact of the waveguide width variations is smaller ($\approx 0.5 \text{ nm}$). As discussed before, since $\frac{\partial n_{eff}}{\partial \lambda} \neq 0$, any alteration in the effective index and resonance wavelength is related: any changes in the effective index influence the resonance wavelength, and as the resonance wavelength changes, it impacts the effective index. As a result, we can expect the variations in the FSR not to be significant. This makes sense also from the point that with any shift in the resonance wavelengths, the wavelength range among those wavelengths (i.e., the FSR) remains almost the same, given that the resonance wavelength shifts at different wavelengths are almost equal.

Employing (15) and (16), Fig. 8 indicates how the cross-over length and coefficients in an MR-based add-drop filter (see Fig. 3(a)) vary with the variations in the silicon thickness and waveguide width. As can be seen from Fig. 8(a), the cross-over length increases as ρ_t increases and $\rho_w = 0$. However, when ρ_w increases and $\rho_t = 0$, the cross-over length decreases. Note

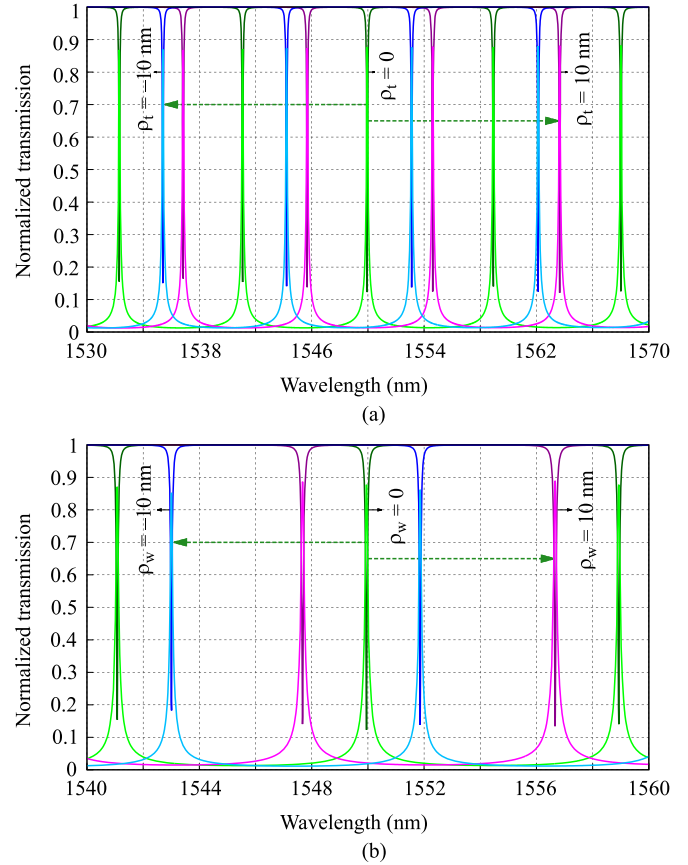


Fig. 9. Optical spectrum of an MR-based add-drop filter when $\rho_{t/w} = \pm 10 \text{ nm}$ calculated using the proposed method ($r \approx 9 \mu\text{m}$ and $l_c = 4 \mu\text{m}$). (a) Under thickness variations ($\rho_w = 0$); and, (b) under width variations ($\rho_t = 0$).

that as the waveguide width increases, the gap between the input waveguide and MR ($2g$ in Fig. 3(b) and (c)) decreases. As a result, the cross-over length, over which the optical power couples from the input waveguide to the MR, decreases as the waveguides get closer. Nevertheless, the gap does not vary with the variations in the silicon thickness. Similarly, in Fig. 8(b) that considers a coupler length of $10 \mu\text{m}$ (i.e., $l_c = 10 \mu\text{m}$), the cross-over coupling coefficient increases as ρ_w increases (i.e., more power can be coupled as the waveguides get wider) and it decreases as ρ_t increases.

Considering (18a) and (18b), Fig. 9(a) and (b) indicate the through and drop ports responses of an MR-based add-drop filter under $\rho_{t/w} = \pm 10 \text{ nm}$, in which $r \approx 9 \mu\text{m}$ and $l_c = 4 \mu\text{m}$ considered to better indicate the shifts (similar to Fig. 7(b)). Also, for better illustration, we excluded the numerical simulation results in the figure, but the average error rate is still smaller than 1% (compare the simulation results in Fig. 11(b) in the next section). The initial resonance wavelength, λ_{MR}^0 , is 1550 nm , and the FSR is $\approx 9 \text{ nm}$. When $\rho_{t/w} > 0$, there is a red-shift in the resonance wavelength, while $\rho_{t/w} < 0$ results in a blue-shift in the resonance wavelength. Furthermore, in Fig. 9(a), the resonance wavelength shift is larger than the FSR (i.e., $\Delta\lambda_{MR} > \text{FSR}$). Another important observation is that there is a good agreement

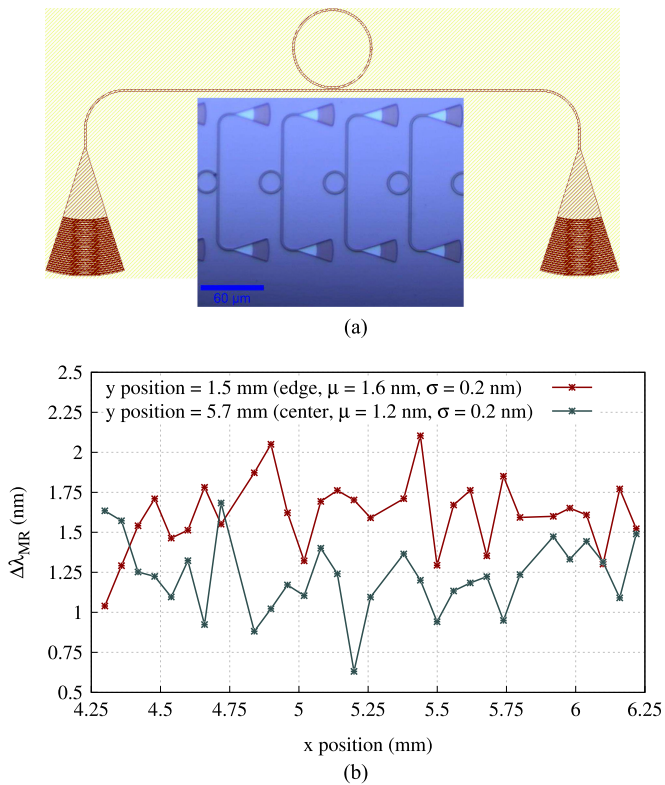


Fig. 10. (a) The unit cell of the fabricated MR (top) with a microscopic photo from part of the chip; and, (b) resonance wavelength shift versus the physical position of the MRs (x and y) when $\lambda_{MR}^0 = 1550$ nm. μ and σ , respectively, denote the average and the standard deviation associated with the resonance wavelength shift.

between the results in Fig. 7(a), which is based on (13), and those indicated in Fig. 9(a) and (b).

Compared with the numerical simulations results indicated for the component and device levels in this section, we demonstrate that our proposed method has a high accuracy with an average error rate smaller than 1%. Most importantly, one of the major advantages of using the proposed method is its low-computation cost. Performing all the quantitative simulation results in this section, we compare the computation time of our proposed method with that of MODE on a PC computer with 2.66 GHz Intel Core i5 CPU and 8 GB of RAM. As indicated in Table I, while MODE performed the simulations in more than two hours, the proposed method computed the results in several seconds, more than 100 times faster than the numerical simulation. The high-accuracy and low-computation cost of our proposed method enables its application to study large-scale SPIs under process variations, where employing time-consuming numerical simulations is not feasible.

B. Fabrication Results and Analysis

We designed an MR-based all-pass filter to demonstrate process variations in silicon photonics fabrication. Sixty identical copies of the designed MR were placed on an 8.8×8.8 mm² chip fabricated by the Electron Beam (EBeam) Lithography System at the University of Washington. Within this chip size, our design space accounted for 2.1×4.5 mm². The MRs were

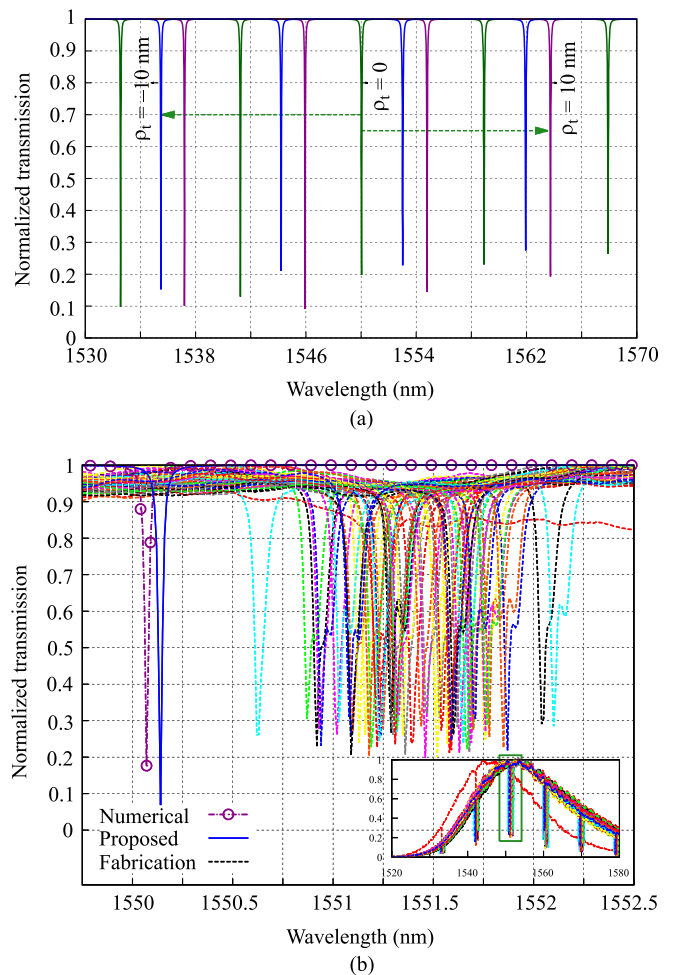


Fig. 11. (a) Optical spectrum of our fabricated TE polarization MR calculated using the proposed method when $\rho_t = 0$ and also when $\rho_t = \pm 10$ nm; and, (b) fabrication results obtained by automatically testing all the MRs, as well as the simulation results from MODE and the proposed method both with $\rho_t/w = 0$.

placed between 60 μ m and 4.2 mm apart, among which thirty MRs were placed at $y = 1.5$ mm near to the edge of the chip and the remaining ones were placed at $y = 5.7$ mm near to the center of the chip (see Fig. 10(b)). The unit cell of the designed MR with a pair of fiber grating couplers, which are designed for 1550 nm quasi-TE operation and are located on a 127 μ m pitch, is depicted in Fig. 10(a). Also, a microscopic photo from part of the chip is indicated in this figure. Our design includes 220 nm thick SOI strip waveguides with a 500 nm width connected to a TE polarization MR with a 10 μ m radius, and a coupler length and gap of ≈ 1 μ m and 200 nm, respectively.

Using an automated probe station at University of British Columbia [35], the MRs were carefully characterized. Furthermore, during the test process, the chip was located on a thermal heater to eliminate the impact of thermal variations. The resonance wavelength shift was found to be smaller than the FSR of the MR. Fig. 10(b) indicates the resonance wavelength shift (i.e., $\Delta\lambda_{MRi} = \lambda_{MRi} - \lambda_{MR}^0$ for $i \in [1, 60]$, where $\lambda_{MR}^0 = 1550$ nm) versus the physical position of the MRs on the chip (i.e., x and y). As can be seen from our experimental results, on average, the resonance wavelength shift for the MRs located close to the chip

TABLE I
COMPUTATION TIME COMPARISON BETWEEN THE NUMERICAL SIMULATION
AND OUR PROPOSED METHOD

Method	Computation time	Average error rate
Numerical (MODE)	128 min	–
Proposed	54 s	1%

center is smaller by 400 pm compares to the MRs located close to the edge of the chip. Fig. 10(b) also indicates the average, μ , and the standard deviation, σ , associated with the resonance wavelength shift: $\mu = 1.6$ nm and $\sigma = 0.2$ nm for the MRs located close to the chip edge, while $\mu = 1.2$ nm and $\sigma = 0.2$ nm for the MRs close to the chip center. We can attribute the deviations to the thickness variation as we found out that $\rho_t > \rho_w$ [6], [11], [17] (see also Fig. 7(a)). Since $\Delta\lambda_{MR} > 0$, based on our study $\rho_t > 0$ in our fabricated chip. The worst- and best-case $\Delta\lambda_{MR}$ (ρ_t) are found to be 2.1 (1.6) and 0.6 (0.5) nm, respectively.

Employing (19), the optical spectrum of the fabricated MR is depicted in Fig. 11(a), in which we consider $\rho_t = 0$ and also $\rho_t = \pm 10$ nm. Furthermore, Fig. 11(b) indicates the measured results obtained by automatically testing all the MRs (60 in total). For easier comparison, this figure also indicates the through port response of the MR around the optical wavelength 1550 nm calculated using our proposed method and MODE, for which $\rho_{t/w} = 0$. As the figure indicates, although all the MRs are identically designed, there is a variation in the resonance wavelengths of the MRs placed at different locations of the chip (see the dashed lines in Fig. 11(b)). Comparing the fabrication and simulation results, we can see that, in the worst-case, there is a 2.1 nm shift in the resonance wavelength of the MR (same as Fig. 10(b)). Comparing all the MRs within the same distance, we found out that the differences in the resonance wavelengths increase with the distance among MRs. The same conclusion was demonstrated in [6], [13].

It is worth mentioning that the mask-less EBeam lithography has a high resolution, but a low throughput, limiting its usage to low-volume production of semiconductor devices which is more suitable for research and development. Other works that considered mask-based optical lithography demonstrated much larger resonance wavelength shifts in MRs due to process variations (see our discussion in Section II). However, even with a small variation, the performance of the system can be highly affected, as we indicate in the next section.

C. System Level Results

In this section, we utilize the analytical models presented in Section VI to evaluate the OSNR of the proposed general passive WDM-based SPI, indicated in Fig. 5, under the variations in the silicon thickness and waveguide width. Different from the previous sections and similar to [6], our system level simulations consider simultaneous random silicon thickness and waveguide width variations with standard deviations of $\sigma_t = 1$ nm and $\sigma_w = 5$ nm, respectively. Moreover, we assume that the variations decrease as we move towards the center of the die.

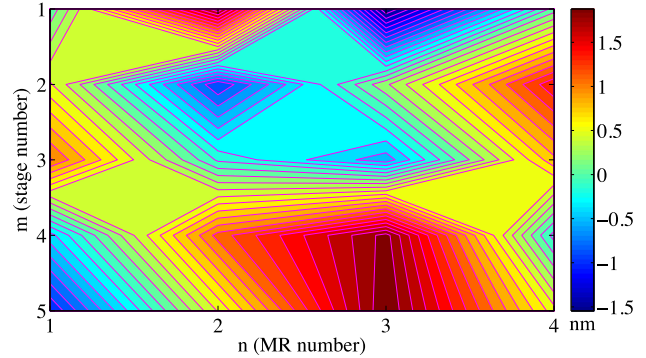


Fig. 12. Random thickness variations contours with $\sigma_t = 1$ nm introduced to a WDM-based SPI with $m = 4$ and $n = 4$. $m = 5$ is the stage at which the photodetectors are located (see Fig. 5).

As an example, Fig. 12 shows the random thickness variations introduced to a WDM-based SPI with $m = 4$ (y-axis) and $n = 4$ (x-axis) and when $\sigma_t = 1$ nm. Please note that $m = 5$ indicates the stage at which the drop filters for the photodetectors are located (see Fig. 5). Similar to the previous sections, the central laser wavelength is 1550 nm. We consider MRs of radii $4 \mu\text{m}$ with couplers with a length of $4 \mu\text{m}$, and hence an FSR of ≈ 17 nm. Moreover, a channel spacing of 2 nm is considered. As discussed before, each MR's radius is slightly different to cover the whole wavelength range. We assume that the optical power at the input port in Fig. 5 (P_{in} in (24a) and (25)) equals 0 dBm. It is worth mentioning that the main purpose of this section is to demonstrate the impact of process variations at the system level (i.e., the system in Fig. 5), and how such variations contribute to the power loss and crosstalk in SPIs.

Employing (24a) and (25), Fig. 13(a) and (b) indicate the desired signal and crosstalk noise power received (i.e., before detection) at each photodetector (x-axis) in a passive WDM-based SPI with $m = 4$ and $n = 4$. When there are no variations (i.e., $\sigma_{t/w} = 0$), as shown in Fig. 13(a), the desired signal power received at different photodetectors is much higher than the crosstalk noise power. Note that even with no variations the crosstalk noise still exists as demonstrated in [32], [36]. On average, the received signal power is -4.2 dBm, while the crosstalk noise power equals -26.5 dBm. The average passing and drop loss for a single MR in our simulations, when no process variations exist, are 0.2 dB and 0.4 dB, respectively. When the variations are introduced, however, both the received desired signal power and crosstalk noise power decrease (see Fig. 13(b)). When the silicon thickness and waveguide width vary, the resonance wavelengths of the MRs shift. Consequently, the MRs fail to precisely switch optical signals at the desired optical wavelengths at each stage, and hence the received signal power at each photodetector drops considerably while some crosstalk will accumulate on the desired optical signal through different MRs at different stages. Nevertheless, the accumulated crosstalk on the desired optical signal also deviates, and hence the received crosstalk noise power is reduced at some of the photodetectors. As Fig. 13(b) indicates, on average, the desired signal power and crosstalk noise power are -23.9 and -27.1 dBm, respectively.

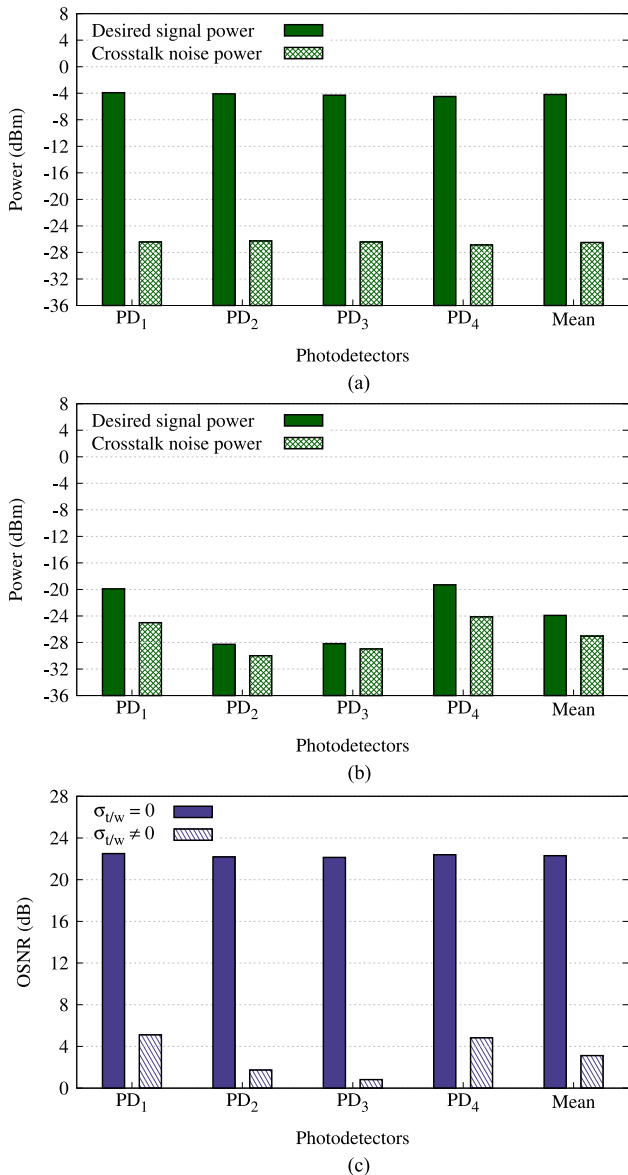


Fig. 13. Desired signal and crosstalk noise power when, (a), $\sigma_{t/w} = 0$ and when, (b), $\sigma_{t/w} \neq 0$, as well as the OSNR, (c), in a passive WDM-based SPI with $m = 4$ and $n = 4$ (see Fig. 5).

Utilizing (26), Fig. 13(c) depicts the OSNR of the network when there are no variations (i.e., $\sigma_{t/w} = 0$) and when the variations exist (i.e., $\sigma_{t/w} \neq 0$). As expected, the OSNR decreases when the variations are introduced. On average, the OSNR is equal to 22.3 dB when $\sigma_{t/w} = 0$, and it drops to 3.1 dB when $\sigma_t = 1$ nm and $\sigma_w = 5$ nm. Considering the results in Fig. 13, when $\sigma_{t/w} \neq 0$ and assuming a heater efficiency of 0.8 mW/FSR [37], an average power consumption overhead of 3.2 mW should be considered to align the resonance wavelengths of the MRs. The results in this section indicate that fabrication process variations can severely degrade the OSNR of SPIs.

VIII. CONCLUSION

In this paper, we present a computationally efficient and accurate bottom-up approach to study random process variations

in large-scale passive WDM-based SPIs. We study the impact of silicon thickness and waveguide width variations on strip waveguides (component level), and also on MR-based add-drop filters and switches (device level). Utilizing the proposed models at the component and device levels, we develop the analytical models required to study the impact of fabrication process variations on the OSNR of a general passive WDM-based SPI, which can be applied to different passive SPI architectures. Compared with time-consuming numerical simulations, we demonstrate that our proposed method has a high accuracy with an average error rate smaller than 1% and a speed-up greater than 100×. Furthermore, we indicate a substantial reduction in the OSNR of passive WDM-based SPIs under silicon thickness and waveguide width variations. Our study also includes the design, fabrication, and analysis of several MRs to demonstrate process variations in silicon photonics fabrication. Utilizing our proposed method, we find out that the worst-case resonance wavelength shift on the fabricated chip is more than 2 nm. The proposed method in this work can be integrated into different silicon photonics design tools, enabling the real-time performance evaluation of SPIs under process variations.

The next step would be to study the impact of different process variations on active SPIs, in which rib waveguides are widely used for constructing different electro-optic devices (i.e., active silicon photonic devices).

REFERENCES

- [1] M. Fiorentino, Z. Peng, N. Binkert, and R. Beausoleil, "Devices and architectures for large scale integrated silicon photonic circuits," in *Proc. IEEE Winter Topicals*, Jan. 2011, pp. 131–132.
- [2] D. Vantrease, R. Schreiber, M. Monchiero, M. McLaren, N. Jouppi, M. Fiorentino, A. Davis, N. Binkert, R. Beausoleil, and J. Ahn, "Corona: System implications of emerging nanophotonic technology," in *Proc. Int. Symp. Comput. Arch.*, Jun. 2008, pp. 153–164.
- [3] Y. Pan, J. Kim, and G. Memik, "FlexiShare: Channel sharing for an energy-efficient nanophotonic crossbar," in *Proc. IEEE Int. Symp. High Performance Comput. Arch.*, Jan. 2010, pp. 1–12.
- [4] S. Le Beux, J. Trajkovic, I. O'Connor, G. Nicolescu, G. Bois, and P. Paulin, "Optical ring network-on-chip (ORNoC): Architecture and design methodology," in *Proc. Design, Autom. Test Eur. Conf. Exhib.*, Mar. 2011, pp. 1–6.
- [5] S. Koohi and S. Hessabi, "All-optical wavelength-routed architecture for a power-efficient network on chip," *IEEE Trans. Comput.*, vol. 63, no. 3, pp. 777–792, Mar. 2014.
- [6] L. Chrostowski, X. Wang, J. Flueckiger, Y. Wu, Y. Wang, and S. T. Fard, "Impact of fabrication non-uniformity on chip-scale silicon photonic integrated circuits," presented at the Opt. Fiber Commun. Conf, San Francisco, CA, USA, 2014, paper Th2A.37.
- [7] L. Chrostowski and M. Hochberg, *Silicon Photonics Design From Devices to Systems*. Cambridge, U.K.: Cambridge Univ. Press, May 2015.
- [8] K. Yee, "Numerical solution of initial boundary value problems involving Maxwell's equations in isotropic media," *IEEE Trans. Antennas Propagation*, vol. 14, no. 3, pp. 302–307, May 1966.
- [9] M. Nikdast, G. Nicolescu, J. Trajkovic, and O. Liboiron-Ladouceur, "Modeling fabrication non-uniformity in chip-scale silicon photonic interconnects," in *Proc. Design Autom. Test Eur. Conf. Exhib.*, Mar. 2016, pp. 115–120.
- [10] M. Nikdast, G. Nicolescu, J. Trajkovic, and O. Liboiron-Ladouceur, "Photonic integrated circuits: A study on process variations," presented at the Opt. Fiber Commun. Conf, Anaheim, CA, USA, 2016, Paper W2A.22.
- [11] W. A. Zortman, D. C. Trotter, and M. R. Watts, "Silicon photonics manufacturing," *Opt. Express*, vol. 18, no. 23, pp. 23598–23607, Nov. 2010.
- [12] A. Krishnamoorthy *et al.*, "Exploiting CMOS manufacturing to reduce tuning requirements for resonant optical devices," *IEEE Photon. J.*, vol. 3, no. 3, pp. 567–579, Jun. 2011.

- [13] X. Chen, M. Mohamed, Z. Li, L. Shang, and A. R. Mickelson, "Process variation in silicon photonic devices," *Appl. Opt.*, vol. 52, no. 31, pp. 7638–7647, Nov. 2013.
- [14] S. Selvaraja, E. Rosseel, L. Fernandez, M. Tabat, W. Bogaerts, J. Hautala, and P. Absil, "SOI thickness uniformity improvement using corrective etching for silicon nano-photonic device," in *Proc. IEEE Int. Conf. Group IV Photon.*, Sep. 2011, pp. 71–73.
- [15] S. Selvaraja, W. Bogaerts, P. Dumon, D. Van Thourhout, and R. Baets, "Subnanometer linewidth uniformity in silicon nanophotonic waveguide devices using CMOS fabrication technology," *IEEE J. Selected Topics Quantum Electron.*, vol. 16, no. 1, pp. 316–324, Jan. 2010.
- [16] X. Wang, W. Shi, H. Yun, S. Grist, N. A. F. Jaeger, and L. Chrostowski, "Narrow-band waveguide bragg gratings on SOI wafers with CMOS-compatible fabrication process," *Opt. Express*, vol. 20, no. 14, pp. 15547–15558, Jul. 2012.
- [17] R. G. Beausoleil, A. Faraon, D. Fattal, M. Fiorentino, Z. Peng, and C. Santori, "Devices and architectures for large-scale integrated silicon photonics circuits," *Proc. SPIE*, vol. 7942, pp. 794204-1–794204-6, 2011.
- [18] Y. Xing, D. Spina, A. Li, T. Dhaene, and W. Bogaerts, "Stochastic collocation for device-level variability analysis in integrated photonics," *Photon. Res.*, vol. 4, no. 2, pp. 93–100, Apr. 2016.
- [19] Y. Xu, J. Yang, and R. Melhem, "Tolerating process variations in nanophotonic on-chip networks," in *Proc. Annu. Int. Symp. Comput. Arch.*, Jun. 2012, pp. 142–152.
- [20] Y. Xu, J. Yang, and R. Melhem, "BandArb: Mitigating the effects of thermal and process variations in silicon-photonic network," in *Proc. 12th ACM Int. Conf. Comput. Frontiers*, May 2015, pp. 30-1–30-8.
- [21] M. Mohamed, Z. Li, X. Chen, L. Shang, and A. Mickelson, "Reliability-aware design flow for silicon photonics on-chip interconnect," *IEEE Trans. Very Large Scale Integr. Syst.*, vol. 22, no. 8, pp. 1763–1776, Aug. 2014.
- [22] Z. Li *et al.*, "Reliability modeling and management of nanophotonic on-chip networks," *IEEE Trans. Very Large Scale Integr. Syst.*, vol. 20, no. 1, pp. 98–111, Jan. 2012.
- [23] E. A. J. Marcatili, "Dielectric rectangular waveguide and directional coupler for integrated optics," *Bell Syst. Tech. J.*, vol. 48, no. 7, pp. 2071–2102, 1969.
- [24] W. J. Westerveld, S. M. Leinders, K. W. A. van Dongen, H. P. Urbach, and M. Yousefi, "Extension of Marcatili's analytical approach for rectangular silicon optical waveguides," *J. Lightw. Technol.*, vol. 30, no. 14, pp. 2388–2401, Jul. 2012.
- [25] A. Yariv and P. Yeh, *Photonics: Optical electronics in modern communications* (The Oxford Series in Electrical and Computer Engineering). London, U.K.: Oxford Univ. Press, 2007.
- [26] D. F. Edwards and E. Ochoa, "Infrared refractive index of silicon," *Appl. Opt.*, vol. 19, no. 24, pp. 4130–4131, Dec. 1980.
- [27] W. Bogaerts, P. De Heyn, T. Van Vaerenbergh, K. De Vos, S. Kumar Selvaraja, T. Claes, P. Dumon, P. Bienstman, D. Van Thourhout, and R. Baets, "Silicon microring resonators," *Laser Photon. Rev.*, vol. 6, no. 1, pp. 47–73, Jan. 2012.
- [28] W. S. C. Chang, *Principles of Optics for Engineers*. Cambridge, U.K.: Cambridge Univ. Press, 2015.
- [29] K. S. Chiang, *Integrated Optic Waveguides*. Hoboken, NJ, USA: Wiley, 2001.
- [30] H. A. Haus, W. P. Haug, S. Kawakami, and N. A. Whitaker, "Coupled-mode theory of optical waveguides," *J. Lightw. Technol.*, vol. LT-5, pp. 16–23, Jan. 1987.
- [31] B. Little, S. Chu, H. Haus, J. Foresi, and J.-P. Laine, "Microring resonator channel dropping filters," *J. Lightw. Technol.*, vol. 15, no. 6, pp. 998–1005, Jun. 1997.
- [32] M. Nikdast *et al.*, "Crosstalk noise in WDM-based optical networks-on-chip: A formal study and comparison," *IEEE Trans. Very Large Scale Integr. Syst.*, vol. 23, no. 11, pp. 2552–2565, Nov. 2015.
- [33] Lumerical Solutions, Inc. [Online]. Available: <http://www.lumerical.com/tcad-products/mode> Accessed on: Jan., 2016.
- [34] T. Alasaarela, D. Korn, L. Alloatti, A. Säynätjoki, A. Tervonen, R. Palmer, J. Leuthold, W. Freude, and S. Honkanen, "Reduced propagation loss in silicon strip and slot waveguides coated by atomic layer deposition," *Opt. Express*, vol. 19, no. 12, pp. 11529–11538, Jun. 2011.
- [35] "UBC (University of British Columbia) automated probe station," [Online]. Available: <http://www.siepic.ubc.ca/probestation>. Accessed on: Feb., 2015.
- [36] M. Bahadori, D. Nikolova, S. Rumley, C. P. Chen, and K. Bergman, "Optimization of microring-based filters for dense WDM silicon photonic interconnects," in *Proc. IEEE Opt. Interconnects Conf.*, Apr. 2015, pp. 84–85.
- [37] T. Y. Liow *et al.*, "Silicon optical interconnect device technologies for 40 Gb/s and beyond," *IEEE J. Sel. Topics Quantum Electron.*, vol. 19, no. 2, Mar/Apr. 2013, Art. no. 8200312.

Mahdi Nikdast (S'10–M'14) received the Ph.D. degree in electronic and computer engineering from The Hong Kong University of Science and Technology, Clear Water Bay, Hong Kong, in 2013. He is a Postdoctoral fellow in the Department of Computer and Software Engineering, Polytechnique Montreal, Montreal, QC, Canada. He is the author or coauthor of 18 peer-reviewed journal papers and 32 papers in conference proceedings. His research interests include silicon photonics, embedded and computing systems, multiprocessor systems, and computer architecture. Related to this work, he received the Best Paper Award from the Design, Automation, and Test in Europe Conference (DATE-2016) and the Best Poster Paper Award from the Asia Communications and Photonics Conference (ACP-2015).

Gabriela Nicolescu received the B.Eng. degree in electrical engineering from Poytechnic University Bucharest, Bucharest, Romania, and the Ph.D. degree from the Institut National Polytechnique de Grenoble, Grenoble, France, in 1998 and 2002, respectively. She is a Professor at Polytechnique Montreal, Department of Software and Computer Engineering. Her research interests include the design methodologies, programming models, and security for advanced heterogeneous systems on chip integrating advanced technologies such as optical networks on chip or liquid cooling systems. She has co-authored more than 160 papers including journal articles, conference papers, books, book chapters, and patents.

Jelena Trajkovic received the M.Sc. and Ph.D. degrees in computer science from the University of California, Irvine, CA, USA, and the Dipl. Ing. degree in electrical engineering from the School of Electrical Engineering (ETF), University of Belgrade, Belgrade, Serbia. Since July 2012, she has been an Assistant Professor at the Department of Electrical and Computer Engineering, Concordia University, Montreal, Canada. She was a Postdoctoral Researcher at Ecole Polytechnique de Montreal and received the ReSMiQ Postdoctoral Fellowship in 2010. Her research interests include silicon photonics, network on chip, embedded systems, and application specific processors.

Odile Liboiron-Ladouceur (M'95–SM'14) received the B.Eng. degree in electrical engineering from McGill University, Montreal, QC, Canada and the M.Sc. and Ph.D. degrees in electrical engineering from Columbia University, New York, NY, USA, in 1999, 2003, and 2007, respectively. She is currently an Associate Professor at the Department of Electrical and Computer Engineering, McGill University. She holds the Canada Research Chair in Photonics Interconnect. Her research interests include optical interconnection networks, data communication systems, photonic integrated circuits, and photonic interconnects. She is the author or coauthor of 40 peer-reviewed journal papers and 85 papers in conference proceedings.